*R*esearch in
*A*stronomy and
*A*strophysics

Numerical simulation of radio signal from extended air showers *

Wei Liu[1,2] and Xuelei Chen[1,3]

[1] National Astronomical Observatories, Chinese Academy of Science, Beijing 100012, China;
    xuelei@cosmology.bao.ac.cn
[2] University of Chinese Academy of Sciences, Beijing 100049, China
[3] Center of High Energy Physics, Peking University, Beijing 100871, China

Abstract The burst of radio emission by an extensive air shower provides a promising alternative for detecting ultra-high energy cosmic rays. We have developed an independent numerical program to simulate these radio signals. Our code is based on a microscopic treatment, with both the geosynchrotron radiation and charge included. Here we give the first presentation of our basic program and its results. When the time-domain signals for different polarizations are computed, we find that the pulses take on a bipolar pattern and the spectrum is suppressed towards the lower frequencies. We investigate how showers at different heights in the atmosphere contribute to the total signal, and examine the signal strength and distribution at sites with different elevations. We also study the signal from showers with different inclination angles and azimuth directions. In all these cases we find the charge excess effect is important.

Key words: astroparticle physics — radiation mechanisms: general

1 INTRODUCTION

It is well-known that high energy cosmic ray particles can produce a large amount of secondary particles when they enter the atmosphere through cascading reactions with air molecules. These ensuing particles are called an *Extensive Air Shower* (EAS). In 1965, radio emissions from these shower particles were detected for the first time (Jelley et al. 1965). This radio signal offers a way to detect very high energy cosmic rays. Later, more experiments were carried out in order to further unravel the characteristics of this radio signal. For a review of these early activities, see Allan (1971). This radio detection technique has several advantages: it can operate round-the-clock with very little dead time, it is highly cost-effective, hence a very large effective collecting area can be achieved, and it is sensitive to the atmospheric depth of the shower maximum (Huege & Pierre Auger Collaboration 2010). However, during the 1970s, as other techniques matured and were considered more reliable at the time, research in this area dwindled.

In the last decade, with fast electronics and high-performance computers appearing, there has been a revival of interest in radio detection of cosmic rays air-showers. The LOFAR PrototypE

Station (LOPES) (Falcke et al. 2005; Schröder et al. 2013; Apel et al. 2013) in Germany and the COsmic ray Detection Array with Logarithmic ElectroMagnetic Antennas (CODALEMA) (Ardouin et al. 2009) in France projects have experimented with radio detection of very high energy cosmic ray particles, and a new generation of radio detectors, called the Auger Engineering Radio Array (AERA), is currently under construction at the site of the Pierre Auger Observatory in South America (Huege & Pierre Auger Collaboration 2010; Schoorlemmer & Pierre Auger Collaboration 2012; Ardouin et al. 2011). In the wake of success of the LOPES project, cosmic ray detection appeared on the agenda of the LOw Frequency ARray (LOFAR). In Yakutsk, Russia, radio arrays for similar purposes (Knurenko et al. 2013) have been built. A series of radio experiments (Ardouin et al. 2011; Martineau-Huynh et al. 2012), called "TREND," has been launched by a Sino-French team to search for ultra-high energy neutrinos, on the site of the 21 Centimetre array (21CMA) radio telescope in Xinjiang, China.

The first prediction of radio emission from an EAS was based on the idea that the extra electrons in the shower could produce coherent Cérenkov radiation at radio frequencies (Askaryan 1962; Askar'yan 1965). However, Kahn & Lerche (1966) proposed that the geosynchrotron mechanism– the synchrotron emission of electrons moving in the geomagnetic field– is the main source of radio emission. The radio pulses produced by the coherent geosynchrotron radiation mechanism exhibit an intense polarization effect, which has been confirmed by recent experiments (Ardouin et al. 2009; Apel et al. 2010).

In recent years, a number of different programs have been developed to calculate the radio signal emitted by a given cosmic ray shower. In one approach, the radiation was calculated by assuming a "macroscopic" model for the charge and current distribution in the shower (Scholten et al. 2008; Werner & Scholten 2008). The numerical computing program *MGMR* (de Vries et al. 2010) and *EVA* (Werner et al. 2012) have been developed. In another "microscopic" approach, the radio signal was computed by sampling the shower particles, and summing a coherent superposition that represents the synchrotron emission field of these particles. The numerical program *REAS*[1] was developed along this line (Huege & Falcke 2003, 2005a,b; Ludwig & Huege 2011). Other models have also been proposed, for example *SELFAS* (Marin & Revenu 2012; Marin 2013) and *ZHAireS* (Alvarez-Muñiz et al. 2012). The computations have been fairly complicated, and there were very large differences in the predictions of these programs, with the amplitude differing by as large as a factor of 20, and also qualitatively in both the time domain (unipolar or bipolar pulse) and frequency domain (flat or suppressed low frequency spectrum). Only recently, after the charge excess effect has been included in the computation with "endpoint formalism" (James et al. 2011), the numerical predictions of the various codes began to converge (Huege et al. 2012).

We have developed an independent numerical program to compute the radio signals from an EAS. It is based on a microscopic model of the radio emission, and both the geosynchrotron and charge excess effect have been included. Although the basic approach is to some extent similar to the *REAS* program, it has been independently developed and many details of the implementation are different, hence it can furnish an independent check on the microscopic approach. In this paper, we give an introduction to our formalism and simulation program. We apply our program to study the characteristic distribution of radio pulses and their dependencies on different incident conditions, including the signal at different altitudes. This approach will be the basis for further investigation on radio emission from cosmic ray air showers.

This paper is organized as follows: in Section 2 we derive the electric field from shower particles, where both geosynchrotron radiation and that from the charge excess effect can be clearly distinguished. In Section 3 we describe our scheme for numerical simulation. In Section 4, the simulated results are presented, where both the time-domain signal and frequency spectra are shown. We also study the contribution from the shower at different heights, and give the result for observers

---

[1] *http://www.timhuege.de/reas/*

at different elevations. In addition, we also consider inclined showers and showers coming from different azimuth directions. Finally we summarize our results in Section 5.

2 RADIATION FORMALISM

The canonical derivation of the electric field of a moving charged particle can be found in standard textbooks on electrodynamics (Jackson 1998; Greiner 1998; Melrose & McPhedran 2005). The retarded potentials produced by arbitrarily distributed sources are given by

$$
\begin{aligned}
\phi(\boldsymbol{r}, t) &= \frac{1}{4\pi\varepsilon_0} \int \mathrm{d}t' \mathrm{d}^3\boldsymbol{r}' \rho(\boldsymbol{r}', t') \frac{\delta(t - t' - |\boldsymbol{r} - \boldsymbol{r}'|/c)}{|\boldsymbol{r} - \boldsymbol{r}'|} \,, \\
\boldsymbol{A}(\boldsymbol{r}, t) &= \frac{\mu_0}{4\pi} \int \mathrm{d}t' \mathrm{d}^3\boldsymbol{r}' \boldsymbol{j}(\boldsymbol{r}', t') \frac{\delta(t - t' - |\boldsymbol{r} - \boldsymbol{r}'|/c)}{|\boldsymbol{r} - \boldsymbol{r}'|} \,,
\end{aligned}
\tag{1}
$$

where ε_0 and μ_0 are respectively the permittivity and permeability in free space, and c is the speed of light in free space. Here we neglect the deviation of the refractive index from its vacuum value (unity), and thus the Čerenkov effect is neglected for the present. $\delta(t - t' - |\boldsymbol{r} - \boldsymbol{r}'|/c)/|\boldsymbol{r} - \boldsymbol{r}'|$ is the Green function of the corresponding wave equation (Jackson 1998), $\rho(\boldsymbol{r}', t')$ and $\boldsymbol{j}(\boldsymbol{r}', t')$ are respectively the charge and current density of sources, and $|\boldsymbol{r} - \boldsymbol{r}'|$ gives the distance from source position $\boldsymbol{r}'$ to the observer position $\boldsymbol{r}$.

Charged particles are produced by pair creation or ionization at the shower front, and then move with the shower, contributing to the total radiation. After moving some distance, they may lose their energy suddenly by major collisions, and leave the shower. The contribution to the radiation at both ends may be important and should be taken into account. The source term of a suddenly-created and destroyed moving charge can be written as

$$
\begin{aligned}
\rho(\boldsymbol{r}, t) &= e\delta^3(\boldsymbol{r} - \boldsymbol{x}(t))\theta(t - t_\mathrm{s})\theta(t_\mathrm{e} - t) \,, \\
\boldsymbol{j}(\boldsymbol{r}, t) &= e\boldsymbol{v}\delta^3(\boldsymbol{r} - \boldsymbol{x}(t))\theta(t - t_\mathrm{s})\theta(t_\mathrm{e} - t) \,,
\end{aligned}
\tag{2}
$$

where e is the unit charge and $\boldsymbol{x}(t)$ is the particle's trajectory in the geomagnetic field. $\theta(t)$ is a Heaviside step function, and t_s and t_e respectively denote the starting and ending time of the motion of a charged particle (Marin & Revenu 2012). In order to integrate the δ function in Equation (1), we introduce a new variable $u = t' + |\boldsymbol{r} - \boldsymbol{x}(t')|/c - t$, and being aware of $\mathrm{d}u/\mathrm{d}t' = 1 - \boldsymbol{n} \cdot \boldsymbol{\beta}$, the corresponding Lienard-Wiechert potentials can be obtained,

$$
\phi = \left[\frac{e}{4\pi\varepsilon_0 KR}\theta(t - t_\mathrm{s})\theta(t_\mathrm{e} - t)\right]_\mathrm{ret} \,, \qquad \boldsymbol{A} = \left[\frac{\mu_0 e\boldsymbol{v}}{4\pi KR}\theta(t - t_\mathrm{s})\theta(t_\mathrm{e} - t)\right]_\mathrm{ret} \,,
\tag{3}
$$

where $K = 1 - \boldsymbol{n} \cdot \boldsymbol{\beta}$ and $R = |\boldsymbol{r} - \boldsymbol{x}(t')|$. The quantities on the right hand side have to be evaluated at the retarded time t', which is determined by the retarded relationship $t = t' + R(t')/c$. The electric field is evaluated in terms of the potentials by $\boldsymbol{E} = -\nabla\phi - \frac{\partial \boldsymbol{A}}{\partial t}$, then we have

$$
\boldsymbol{E} = \left\{-\nabla\left[\frac{e}{4\pi\varepsilon_0 KR}\right]_\mathrm{ret} - \frac{\partial}{\partial t}\left[\frac{\mu_0 e\boldsymbol{v}}{4\pi KR}\right]_\mathrm{ret}\right\} [\theta(t - t_\mathrm{s})\theta(t_\mathrm{e} - t)]_\mathrm{ret}
$$

$$
\tag{4}
$$

$$
+ \left\{-\left[\frac{e}{4\pi\varepsilon_0 KR}\right]_\mathrm{ret}\nabla t' - \left[\frac{\mu_0 e\boldsymbol{v}}{4\pi KR}\right]_\mathrm{ret}\frac{\partial t'}{\partial t}\right\}\frac{\partial}{\partial t'}\left[\theta(t - t_\mathrm{s})\theta(t_\mathrm{e} - t)\right]_\mathrm{ret} \,.
$$

Here the first term is due to the continuous motion of charged particles, while the second term accounts for the sudden creation and destruction. Noting that (Griffiths & College 1999),

$$
\frac{\partial t}{\partial t'} = 1 - \boldsymbol{n} \cdot \boldsymbol{\beta} \,, \qquad \nabla t' = -\frac{\boldsymbol{n}}{c \cdot (1 - \boldsymbol{n} \cdot \boldsymbol{\beta})} \,,
\tag{5}
$$

we have

$$\boldsymbol{E}(\boldsymbol{x},t) = \frac{e}{4\pi\epsilon_0}\left\{\left[\frac{(\boldsymbol{n}-\boldsymbol{\beta})}{\gamma^2 K^3 R^2}\right]_{\text{ret}} + \left[\frac{\boldsymbol{n}\times\{(\boldsymbol{n}-\boldsymbol{\beta})\times\dot{\boldsymbol{\beta}}\}}{cK^3 R}\right]_{\text{ret}}\right\}[\theta(t-t_{\text{s}})\theta(t_{\text{e}}-t)]_{\text{ret}}$$
$$+ \left[\frac{e(\boldsymbol{n}-\boldsymbol{\beta})}{4\pi\varepsilon_0 K^2 Rc}\right]_{\text{ret}}\frac{\partial}{\partial t'}[\theta(t-t_{\text{s}})\theta(t_{\text{e}}-t)]_{\text{ret}} . \tag{6}$$

In the braces, the first term is called the generalized Coulomb field and the second term is the well-known radiation field, or acceleration field. The third term indicates the radiation from the particle's creation and destruction. So in a neutral shower, as both positive and negative charges (electrons and positrons) move toward the ground, the net contribution from the third term is nearly zero. However, because electrons from air molecules are knocked out by the cosmic ray and join the shower, a real shower is negatively charged (Askaryan 1962; Askar'yan 1965; Alvarez-Muñiz et al. 2012). This radiation from the excess electrons has a significant contribution to the radiation, as we shall see below, and following others, we will call it the charge excess effect.

When a particle moves in the geomagnetic field, it will continuously undergo Lorentz force and radiate. The radiation formula is

$$\boldsymbol{E}(\boldsymbol{x},t) = \frac{e}{4\pi\epsilon_0}\left\{\left[\frac{(\boldsymbol{n}-\boldsymbol{\beta})}{\gamma^2 K^3 R^2}\right]_{\text{ret}} + \left[\frac{\boldsymbol{n}\times\{(\boldsymbol{n}-\boldsymbol{\beta})\times\dot{\boldsymbol{\beta}}\}}{cK^3 R}\right]_{\text{ret}}\right\}, \tag{7}$$

where ε_0 and μ_0 are respectively the permittivity and permeability of free space, and c is the speed of light in free space. γ is the Lorentz factor, $\boldsymbol{\beta}=\boldsymbol{v}/c$ and $\dot{\boldsymbol{\beta}}=\dot{\boldsymbol{v}}/c$ are respectively the velocity and acceleration of the particle in units of speed of light, $\boldsymbol{n}=(\boldsymbol{r}-\boldsymbol{r}')/|\boldsymbol{r}-\boldsymbol{r}'|$ is the unit vector from the source to the observer and $K=1-\boldsymbol{n}\cdot\boldsymbol{\beta}$. In Equation (7), the first term is called the generalized Coulomb field and the second term is the well-known radiation field or acceleration field. The quantities within the square brackets have to be evaluated according to the retardation relationship $t=t_r+R(t_r)/c$. Here we neglect the deviation of the refractive index from its vacuum value (unity), and thus the Čerenkov effect is neglected for the present. However, in the evolution of an air shower, particles are continuously generated and annihilated and undergo a transient acceleration or deceleration. However, although we do not know exactly the course of acceleration (deceleration), we can still obtain the total radiation field.

$$\int_{t_1}^{t_2}\boldsymbol{E}(\boldsymbol{x},t)\mathrm{d}t = \int_{t_1}^{t_2}\frac{e}{4\pi\epsilon_0}\left[\frac{\boldsymbol{n}\times\{(\boldsymbol{n}-\boldsymbol{\beta})\times\dot{\boldsymbol{\beta}}\}}{cK^3 R}\right]_{\text{ret}}\mathrm{d}t ,$$
$$= \frac{e}{4\pi\epsilon_0 c}\int_{t'_{r1}}^{t'_{r2}}\frac{\boldsymbol{n}\times\{(\boldsymbol{n}-\boldsymbol{\beta})\times\dot{\boldsymbol{\beta}}\}}{K^2 R}\mathrm{d}t_r ,$$
$$= \frac{e}{4\pi\epsilon_0 cR}\int_{t'_{r1}}^{t'_{r2}}\frac{\mathrm{d}}{\mathrm{d}t_r}\left\{\frac{\boldsymbol{n}\times(\boldsymbol{n}\times\boldsymbol{\beta})}{K}\right\}\mathrm{d}t_r ,$$
$$= \frac{e}{4\pi\epsilon_0 cR}\left[\frac{\boldsymbol{n}\times(\boldsymbol{n}\times\boldsymbol{\beta})}{K}\right]\Bigg|_{t_{r1}}^{t_{r2}} . \tag{8}$$

Here we assume that the particle is far from the observer and apply the relationship $\mathrm{d}t/\mathrm{d}t_r = 1-\boldsymbol{n}\cdot\boldsymbol{\beta}$.

3 ALGORITHMS

3.1 Properties of an Extensive Air Shower

The development of the air shower can be simulated with Monte Carlo programs, such as CORSIKA (Heck et al. 1998), AIRES (Sciutto 1999) and COSMOS (Roh et al. 2013). As a first step, in this paper we apply parameterized functions to describe the distribution of shower electrons and positrons, focusing on the relation between the radio signal and properties of the shower, and leave the detailed modeling of the air showers to future work. Here we briefly recall the salient features of these parameterized distribution functions used in the present simulation, which were also used by Huege & Falcke (2003, 2005a).

The "shower age" s is often used as a measure of shower evolution, and a good approximation of it is

$$s(X) = \frac{3X}{X + 2X_m} \, , \tag{9}$$

where s varies between 0 and 3. X is the atmospheric depth, which is defined as an integral of air density along the shower path,

$$X(h) = \int_h^H \frac{\rho(h)}{\cos\theta} \mathrm{d}h \, , \tag{10}$$

where ρ is the atmospheric density, H the initial height of shower development and θ is the zenith angle of the shower. X_m signifies the atmospheric depth where the shower reaches its maximum, viz. $s = 1$, with

$$X_m = X_0 \ln(E_\mathrm{p}/E_\mathrm{c}) \, , \tag{11}$$

where $X_0 = 36.7$ g cm^2 is the radiation length of an electron in the air, which is about 300 m at sea level and $E_\mathrm{c} = 86$ MeV is the critical energy where the ionization loss of the electron equals the radiative loss. Below, as an illustration of the typical case, we shall consider a cosmic-ray proton with primary energy $E_\mathrm{p} = 10^{17}$ eV. The atmosphere density $\rho(h)$ is parameterized according to the US Standard Atmosphere from 1977, where the atmosphere of the Earth is separated into four layers. At layer i

$$\rho(h) = \frac{b_i}{c_i} \exp\left(-\frac{h}{c_i}\right) \, , \tag{12}$$

where the parameters b_i and c_i for different layers are listed in Table 1.

Table 1   Parameters for the Parametrization of Atmospheric Layers (taken from Huege & Falcke 2005a)

Layer	Height (km)	b_i (g cm^{-2})	c_i (cm)
1	$0 - 4$	1222.66	994186.38
2	$4 - 10$	1144.91	878153.55
3	$10 - 40$	1305.59	636143.04
4	$40 - 100$	540.18	772170.16

The profile of shower size, i.e. the total number of electromagnetic components $N(s)$ (including both electrons and positrons) at given shower age s, is parameterized as (Greisen 1960)

$$N(s) = \frac{0.31}{\sqrt{X_m/X_0}} \exp\left[\frac{X_m}{X_0} \frac{2 - 3\ln s}{3/s - 1}\right] \, . \tag{13}$$

The number of particles injected per unit of atmospheric depth dX is then

$$I(X) = \frac{dN(s)}{dX} + \frac{N(s)}{\lambda} \, , \tag{14}$$

where $\lambda \approx 40$ g cm^2 is the mean free path of an electron in the air. The atmospheric depth of a single particle follows an exponential distribution $p(X) \sim \exp(-X/\lambda)$, and $\frac{N(s)}{\lambda}$ is the number of annihilated particles per unit radiation length.

The lateral spread of shower particles comes mainly from Coulomb scattering of electrons off atoms in the air. A favorite expression for the radial distribution of electromagnetic components within the shower is the Nishimura-Kamata-Greisen (NGK) parameterization (Kamata & Nishimura 1958; Greisen 1960)

$$\varrho_{\text{NKG}}(r) = \frac{1}{r_{\text{M}}^2} \cdot \frac{\Gamma(4.5 - s)}{2\pi\Gamma(s)\Gamma(4.5 - 2s)} \left(\frac{r}{r_{\text{M}}}\right)^{s-2} \left(1 + \frac{r}{r_{\text{M}}}\right)^{s-4.5} , \tag{15}$$

where r_{M} is the Moliere radius, which characterizes transverse spreading of the shower disk and is a function of atmospheric depth X (Dova et al. 2003)

$$r_{\text{M}} = \frac{9.6}{(X - a_i)} c_i . \tag{16}$$

Showers that develop at higher altitudes usually have a wider lateral spread.

The thickness of the shower disk can be probed by measuring the arrival time distribution. A useful fitting formula is from Agnetta et al. (1997), which contains both the curvature of the disk and the longitudinal distribution within it

$$f(t) = At^B \exp(-Ct) , \tag{17}$$

where t is the particle's arrival time at the detector relative to the shower front. Parameter A is a normalization, whereas B and C are functions of the mean arrival time $\langle t \rangle$ and corresponding standard deviation σ_t, both of which are related to radial distance to the center of the shower,

$$B = \left(\frac{\langle t \rangle}{\sigma_t}\right)^2 - 1 , \quad C = \frac{\langle t \rangle}{\sigma_t^2} ,$$

$$\langle t \rangle(r), \ \sigma_t(r) = F + G\left(\frac{r}{r_0}\right)^H ,$$

where

$$\begin{aligned}
F_t &= (8.039 \pm 0.068)\text{ns}, & F_\sigma &= (5.386 \pm 0.025)\text{ns} , \\
G_t &= (5.508 \pm 0.095)\text{ns}, & G_\sigma &= (5.307 \pm 0.032)\text{ns} , \\
H_t &= 1.710 \pm 0.059, & H_\sigma &= 1.586 \pm 0.020 .
\end{aligned}$$

The average energy of the electrons and positrons in the air shower is about 30 MeV, where $\gamma \sim 60$ (Allan 1971). Following Huege & Falcke (2003), we parameterize the energy distribution of the cascading electrons as a broken power law, i.e.

$$p(\gamma) = \frac{\gamma}{74.2} \left(1 - e^{-(\gamma/74.2)^{-3}}\right) , \tag{18}$$

where γ denotes the Lorentz factor, which varies from 5 to 1000. In this distribution, its maximum is at $\gamma = 60$.

A typical air shower is not neutral but has more electrons, whose fraction usually varies with atmospheric depth X but has a mean of 23%. Here as a first approximation, we adopt a constant value of 25%.

3.2 Strategy of Numerical Simulation

We use the Monte Carlo technique to simulate the radio emission. Electrons and positrons are generated randomly according to the shower distribution functions in a frame moving with the center of the shower, then their positions in the ground reference frame are obtained by a coordinate transformation (see Appendix A for details). The direction of initial velocity is assumed to be along the radius of the spherical shower surface, and the subsequent motion of the charged particles in the geomagnetic field is calculated according to the Lorentz formula (See Appendix B), where we have neglected the energy loss due to radiation or small angle scattering. We also use the Monte Carlo method to determine the free path of each particle in order to determine where the destruction takes place. To take the radiation from the creation/destruction of the charged particles into account, we need to estimate the number of particles created and destroyed at each atmospheric depth. These are given by the injection rate $I(X)$ as shown in Equation (14) and destruction rate $|N(X)/\lambda|$.

In Figure 1, we plot the number of particles $N(X)$, number of injected particles $I(X)$ and number of annihilated particles $B(X)$ at different atmospheric depths in a vertical shower (coming from the zenith). The shower begins its development high in the atmosphere, the number of particles increases as it moves downward, reaching a maximum at $631 \, \mathrm{g} \, \mathrm{cm}^{-2}$ for a 10^{17}eV cosmic ray proton, i.e. about 4000 m high, then the number of particles begins to decrease. The number of injected particles $I(X)$ reaches a maximum slightly earlier than the total number itself.

The time of emission and time of observation of the signal are related by a nonlinear retardation relation. Along the particle trajectory, a series of points are uniformly sampled and their contribution to the electric field at the corresponding observing time is computed. We approximate the electric field to be $\bar{E}(t_1) = \frac{1}{\Delta t} \int_{t_1}^{t_1+\Delta t} E(t) \mathrm{d}t$. Here Δt is the predefined time resolution, and for each segment a linear approximation is made. At both endpoints of the trajectory, there are extra contributions from the creation or destruction of the particle. In Equation (6), the third term reduces to

$$\left[\frac{e(\boldsymbol{n} - \boldsymbol{\beta})}{4\pi\varepsilon_0 K^2 Rc} \left\{ \delta(t - t_\mathrm{s})\theta(t_\mathrm{e} - t) - \theta(t - t_\mathrm{s})\delta(t_\mathrm{e} - t) \right\} \right]_\mathrm{ret} . \tag{19}$$

To get rid of the δ-function, we can integrate for a very short interval, $\int_{t_\mathrm{s}-\epsilon}^{t_\mathrm{s}+\epsilon} [...]_\mathrm{ret} \mathrm{d}t$, and the end point terms reduce to $\pm \left[\frac{e\,(\boldsymbol{n}-\boldsymbol{\beta})}{4\pi\varepsilon_0 K Rc} \right]_\mathrm{ret}$.
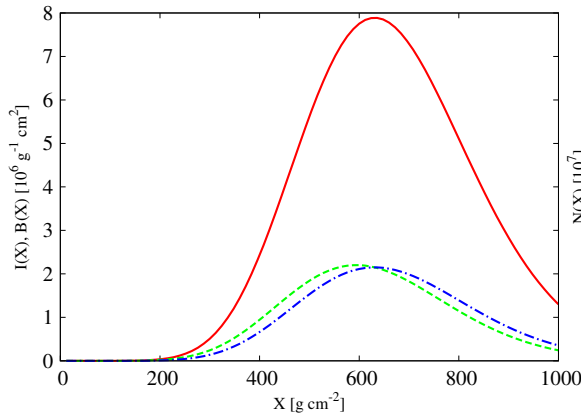
Fig. 1 $N(X)$ (*solid line*): the number of particles of an air shower as a function of height, $I(X)$ (*dashed line*): number of injected particles per unit atmospheric depth, $B(X)$ (*dash-dotted line*): number of annihilated particles per unit atmospheric depth.

For simplification, in our simulation we only generate electrons and positrons which acquire velocity $\sim c$, but neglect the contribution from positively charged ions, which move with very low speed. As $K = 1 - \boldsymbol{n} \cdot \boldsymbol{\beta}$, and the radiation term is proportional to K^{-1}, this approximation is generally good. However, this omission could result in a longitudinal component of polarization when calculating the end point radiation when the electron is "created" by ionization, or "destroyed" by recombination, because it violates charge conservation at the creation and destruction point. This can be avoided by considering the contribution from the ions, which are created or destroyed at the same point. The velocity of such an ion is nearly zero, and the corresponding end point radiation is $\left[\frac{e\,\boldsymbol{n}}{4\pi\varepsilon_0 Rc}\right]_{\text{ret}}$, with the sign just opposite to the electron being created/destroyed. So, the sum of the radiation along the direction of observation is

$$
\begin{aligned}
\pm\left[\frac{e\,(\boldsymbol{n}-\boldsymbol{\beta})}{4\pi\varepsilon_0 KRc} - \frac{e\,\boldsymbol{n}}{4\pi\varepsilon_0 Rc}\right]_{\text{ret}} &= \pm\left[\frac{e\,(\boldsymbol{n}-\boldsymbol{\beta}-(K=1-\boldsymbol{n}\cdot\boldsymbol{\beta})\boldsymbol{n})}{4\pi\varepsilon_0 KRc}\right]_{\text{ret}}, \\
&= \pm\left[\frac{e\,((\boldsymbol{n}\cdot\boldsymbol{\beta})\boldsymbol{n}-\boldsymbol{\beta})}{4\pi\varepsilon_0 KRc}\right]_{\text{ret}}, \\
&= \pm\left[\frac{e\,\boldsymbol{n}\times(\boldsymbol{n}\times\boldsymbol{\beta})}{4\pi\varepsilon_0 KRc}\right]_{\text{ret}}.
\end{aligned}
\tag{20}
$$

Then radiation from the charge excess effect only contains the part whose direction of electric field is perpendicular to the direction of observation. We will use Equation (20) to calculate the end point radiation.

An actual shower of a 10^{17}eV proton primary has about 10^8 shower particles, but in the Monte Carlo simulation only a small fraction of these, usually a few million particles, are sufficient. We estimate the electric field as

$$
\hat{\boldsymbol{E}} = \frac{N}{n}\sum_i^n \boldsymbol{E}_i\,,
\tag{21}
$$

where N and n are the expected total particle number and the sampled particle number respectively. We use an adaptive control to reach the required precision in sampling: in each iteration a batch of 10^5 particles is added to the sample, and estimates of the electric field at all the required locations and time grid points are updated, and compared with the values of the previous iteration. The number of location-time points where the relative change exceeds the required precision (10^{-3}) is recorded. Once such points are less than a predefined number, say 10 in 5000, the result is considered to be stable and the simulation is terminated. Our numerical program is implemented using the C programming language with the aid of the Gnu Scientific Library[2].

4 RESULTS

4.1 The Contribution from Different Radiation Mechanisms

To understand how the different radiation mechanisms work, we calculate the electric field signal from the pure geosynchrotron, the pure charge excess effect, and their combined sum. First we consider a 10^{17} eV vertical shower and a 0.5 G magnetic field pointing due north horizontally. The shower is assumed to have an electron excess of 25%.

The electric field signal at the impact center on the ground is shown in Figure 2, with polarizations in the East-West (EW) direction, North-South (NS) direction and vertical direction, as well as the frequency spectrum for the signal. Under the Lorentz force from the geomagnetic field, the charged particles in the vertical shower are deflected toward east and west. As a result, we expect
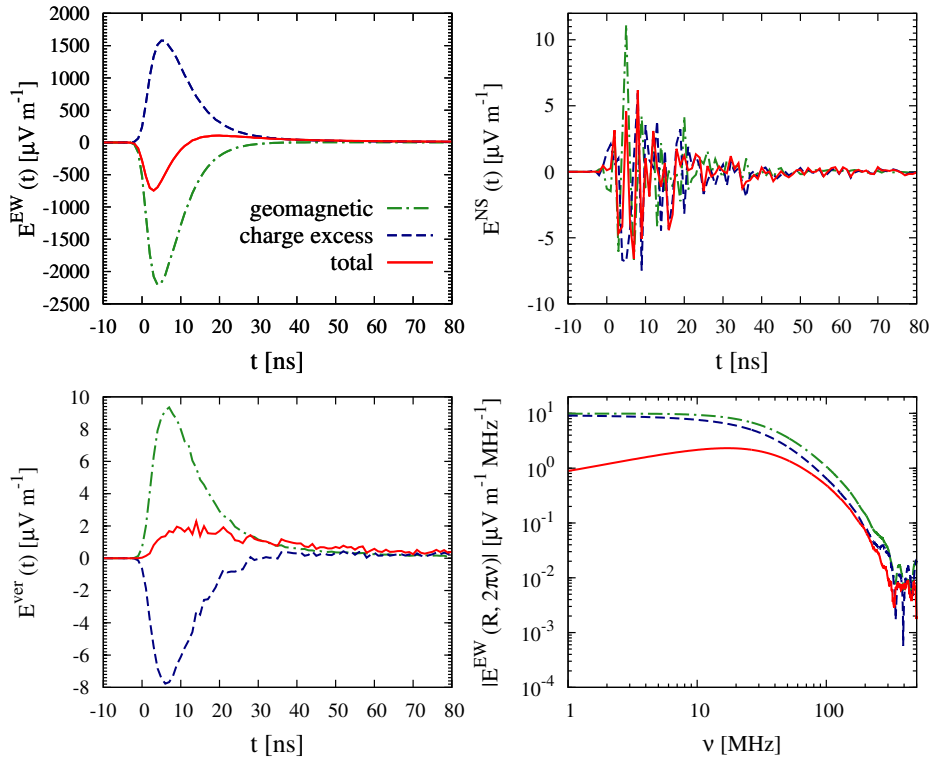
Fig. 2 The three polarization signals (*upper left*: EW, *upper right*: NS, *lower left*: vertical) and the frequency spectrum of the EW polarization (*lower right*) as observed at the center of the shower on the ground, with the pure geosynchrotron (*green dash-dotted curve*), the pure charge excess effect (*blue dashed curve*) and both (*red solid curve*).

a linear polarization in the geosynchrotron radiation in the EW direction, while the NS polarization is expected to be small, and the vertical polarization is expected to vanish as it is along the line of sight. These expectations are confirmed in Figure 2 where a strong pulse in the EW polarization due to the pure geosynchrotron mechanism is shown as the green dash-dotted line in the negative (west), which peaks at 8 ns, with a strength of almost $2000\,\mu$Vm. The NS polarization oscillates with a small amplitude, but the vertical polarization vanishes.

However, when the charge excess effect is included, we see that it makes a prominent and opposite contribution to the total electric field, shown as the blue-dashed curve. As a result, it cancels a large part of the field generated by the geosynchrotron mechanism, especially for the primary EW polarization. The net effect, shown as the red solid curve, is a much reduced pulse, that is only about $400\,\mu$Vm at its peak, and even has a bipolar character where the signal at the later time is reversed in sign with respect to the earlier one, which is different from the unipolar pattern with pure geosynchrotron radiation. Whether the pulse is unipolar or bipolar has been debated and it was only recently resolved that the difference is due to the inclusion of the charge excess effect (Huege et al. 2012). There is also a slight vertical component at the level of $\sim 2 \times 10^{-2}$ in the total signal, probably due to the finite size of the shower disk, and also due to the asymmetry in charge.

Next we consider the signal at off-center locations. In Figure 3, we plot the signals at a site 100 m due north of the ground center (top four panels), and a site 100 m west of the ground center
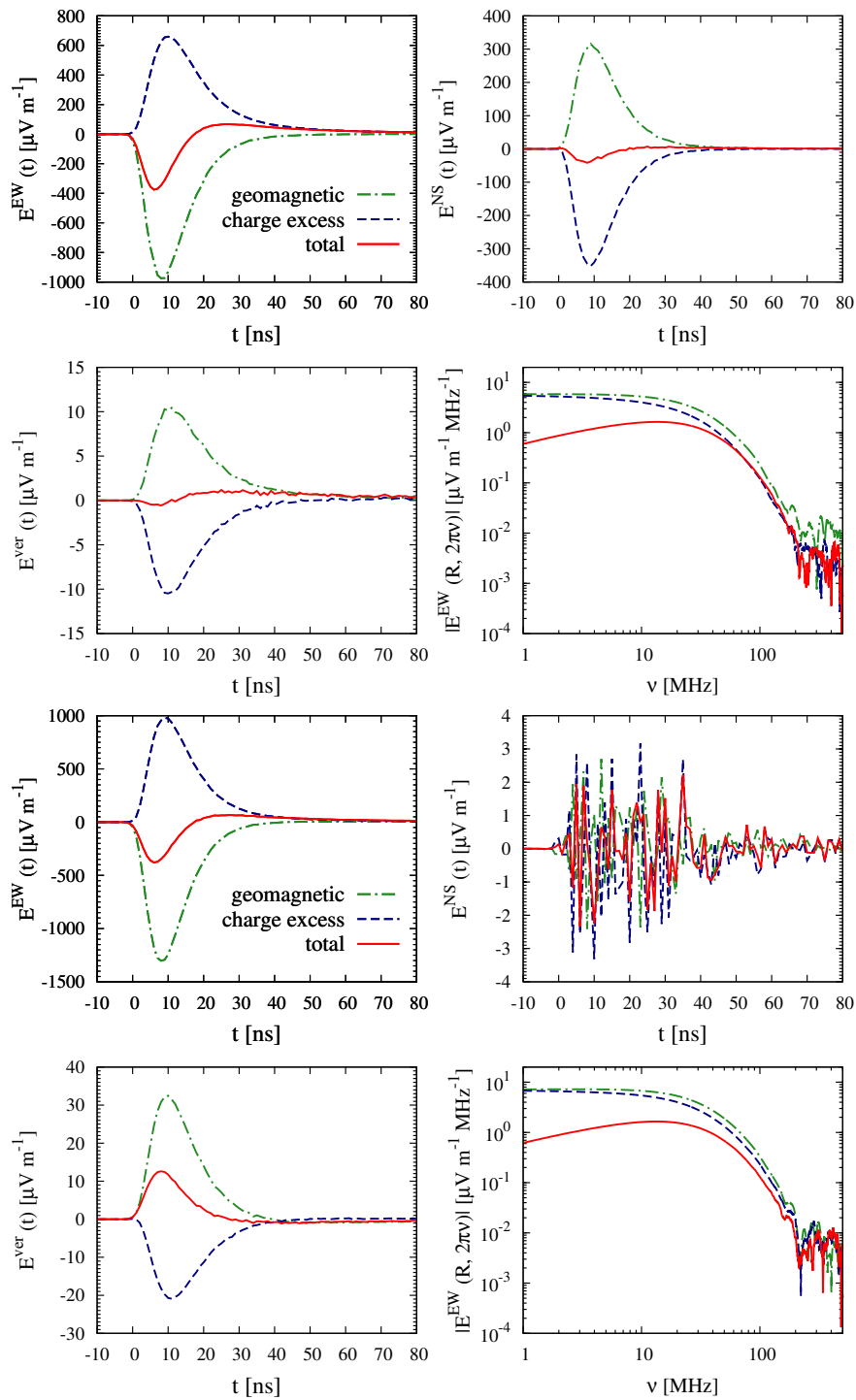
Fig. 3 The same as Fig. 2, except at an off-center site. *Top four panels*: 100 m north of the center of the shower on the ground. *Bottom four panels*: 100 m west of the center of the shower on the ground.
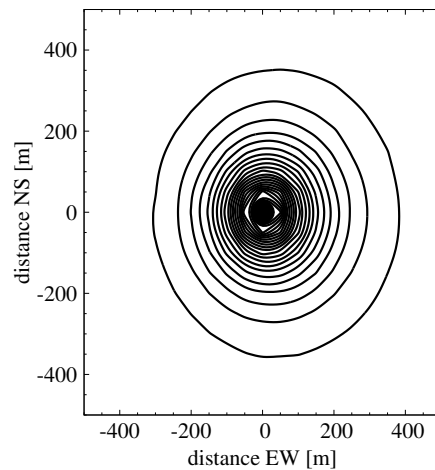
Fig. 4 The contours around the maximum in the electric field in the EW polarization from a vertical shower. The contour levels are $25\ \mu\mathrm{V\ m^{-1}}$ apart.

(bottom four panels). Again, many of the basic features are similar to the case at the ground center, with the EW polarization still being dominant, though the amplitude is smaller than at the ground center. In the off-center case, the NS polarization may be present. Interestingly, in the case of 100 m north, both the pure synchrotron and the charge excess effect alone could produce a relatively large peak, but they nearly cancel each other and the net effect is a relatively small peak.

The whole pattern of the shower signal is shown in Figure 4. The signal is highly beamed, and we can see there is a slight asymmetry in the EW direction. The shower is nearly vertical, but the Lorentz force deflects the motion of particles, and there is a net charge excess in the shower; in the end it produced the pattern as shown in Figure 4.

4.2 Fitting the Frequency Spectra

In Figures 2 and 3, we have also plotted the frequency spectrum of the radiation for different mechanisms (bottom right panels in each of the four-plot combinations). The major component of the radio emission lies in the frequency range of about tens of MHz, in agreement with observations.

At the high frequency end, we see from these figures that for both the geosynchrotron and the charge excess effect, the spectra fall off exponentially above ~ 100 MHz, though the charge excess radiation decays slightly earlier than the geosynchrotron radiation. As a result, the total spectrum also declines. This spectral drop off is due to the loss of coherence, because at such high frequencies the wavelength is far less than the thickness of the shower, and the contributions to the field strength from different parts of the shower no longer simply add up. As a result, the radiation is insignificant at such high frequencies.

At the low frequency end, we can see from these figures that for both the geosynchrotron and charge excess effect, the spectra are nearly flat. However, as the two are oriented in opposite directions, they cancel each other out, and the total signal has a slowly decreasing spectrum at the lower frequencies. This cut off at the lower frequency due to the cancelation effect has been noted in recent literature (Werner & Scholten 2008; Ludwig & Huege 2011; Marin & Revenu 2012; Alvarez-Muñiz et al. 2012).

Experimentally, analyses of a few strong events by the CODALEMA (Ardouin et al. 2006) and LOPES (Nigl et al. 2008; Haungs et al. 2009) projects have shown that in the range $30 - 70$ MHz,
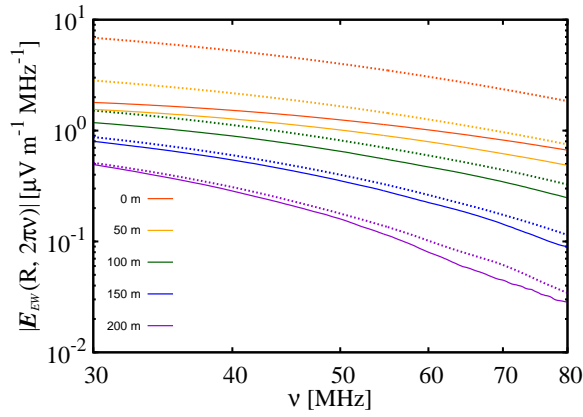
Fig. 5 The frequency spectra at different radial distances to the east of the center of the shower on the ground. From top to bottom, the distances are respectively 0, 50, 100, 150 and 200 m. Short dashed lines: only geosynchrotron radiation; solid lines: with both geosyhchrotron and the charge excess effect.

the frequency spectrum can be well fitted with a single power law $\epsilon_\nu = K \cdot \nu^{-\alpha}$ with spectral index $a = -1 \pm 0.2$, or alternatively by an exponential function $\epsilon_\nu = K \cdot \exp(\nu/\mathrm{MHz}/\beta)$, where β spans the range from -0.021 to -0.013. This is slightly steeper than the slope predicted by the pure geosynchrotron case. In these experiments, they found no significant dependence of the spectral slope on the distance to the shower axis, the zenith angle or the azimuth angle.

In Figure 5 we plot the simulated spectra at different distances from the center on the ground for a vertical shower. Short dashed lines are the spectra for the pure geosynchrotron, while solid lines are those including charge excess effect. From top to bottom, the distances to the center of the shower at impact are respectively 0, 50, 100, 150 and 200 m. We also fit these spectra with a single power law $\epsilon_\nu = E_0 \cdot \nu^{-\alpha}$ in the range $40 - 70$ MHz.

The fitting values of E_0 and α are reproduced in Table 2 for distances measured to both the east and west of the ground center, as there is a slight asymmetry as we noted before. It is apparent that within 150 meters, the single power law is a good fit to the spectrum. With the radial distances increasing, the slope becomes steeper. Near the center part (within 50 m), the slope of the spec-

Table 2 The fitted parameters of the frequency spectrum at different radial distances along the east and west directions. We fit with a single power law $\epsilon_\nu = K \cdot \nu^{-\alpha}$ between $40 - 70$ MHz.

Distance (m)	Orientation	E_0 (pure)	α (pure)	E_0 (both)	α (both)
0	center	1114.72	1.442	96.37	1.114
50	east	1114.72	1.442	161.56	1.301
	west	1403.90	1.565	132.16	1.268
100	east	573.62	1.680	520.54	1.714
	west	2836.44	1.893	410.51	1.681
150	east	2425.63	2.233	3846.32	2.383
	west	10454.02	2.405	3152.25	2.375
200	east	17889.64	2.952	110199.9	3.453
	west	50671.17	3.012	93022.37	3.464

trum including both geosyhchrotron and the charge excess effect is -1 ± 0.2, consistent with the experimental result. On the other hand, for the pure geosynchrotron radiation, the slope α conflicts with experimental results, and the difference is larger than the margin of error. This shows that the inclusion of the charge excess effect is very important.

However, far away from the center, both the pure geosynchrotron model and the model with the charge excess effect predict a steepening of the spectra, but observations so far have not found such a change. Part of this may be due to experimental error, because far from the center of the shower on the ground, the signal strength falls off exponentially, and the resulting measurement error is large. Another possibility is that the Čerenkov radiation may have a visible effect at intermediate distances (de Vries et al. 2012) and may modify the corresponding frequency spectrum.

4.3 Contribution from Different Elevations

We now study how the shower at different heights contributes to the total signal at ground level. If the shower is point-like, there would be a one-to-one relation between the emission time and arrival time for the radio pulse, with the radiation emitted earlier arriving earlier. The envelope of the signal would clearly show this trend in the shower at different heights (Alvarez-Muñiz et al. 2012). However, the real case is more complicated due to the spatial extent of the shower disk, for at any given time, the signal received at a location on the ground (altitude 0) is a superposition of emissions from different parts of the shower at different times. The problem of contribution from different heights in the case of pure geosynchrotron was investigated by Huege et al. (2007); here, we consider the case with the charge excess effect.

We compute contributions to the radio signal at different heights. The results are shown in Figure 6. For illustration, we have chosen two observing sites, one at the center of the shower on the ground and one at 100m-west from the center.

Starting from the ground, we divide the whole atmosphere into seven layers. Each layer occupies an interval of 1200 m, except for the highest one, where we combine all contributions from above 7200 m. We plot the contribution of each layer as well as the total signal. A general impression is that each layer can contribute both to the first, strong (negative) peak as well as the second, weak (positive) peak, though the higher layers contribute more to the first while the lower ones contribute more to the second. The $3600 - 4800\,\mathrm{m}$ and $2400 - 3600\,\mathrm{m}$ layers contribute the largest signal. These two are also the layers which contain the maximum number of particles. The contributions from the higher elevations are smaller but still significant. The contributions of the lower layers ($0 - 1200\,\mathrm{m}$ and $1200 - 2400\,\mathrm{m}$) are also sizeable. They are closer to the observer, but the number of particles has decreased. In particular, the contribution of $0 - 1200\,\mathrm{m}$ is sizeable at the center on the ground, but away from this point it is much less, due to relativistic beaming.

We further compute the contribution from different lateral distances, see Figure 7. The observation site is chosen to be the center of the shower. We make concentric rings around the shower axis, with the first ring within $5\,\mathrm{m}$, then $5 - 10\,\mathrm{m}$, $10 - 20\,\mathrm{m}$, $20 - 30\,\mathrm{m}$, $30 - 50\,\mathrm{m}$, and beyond $50\,\mathrm{m}$, and estimate the contribution from each. The main contribution comes from the distance within $50\,\mathrm{m}$, especially within $5\,\mathrm{m}$. This is because most of the shower particles are located in the inner rings near the center of the shower, as the horizontal motion caused by the geomagnetic field is small compared with the shower velocity.

4.4 Signals from Observing at Different Elevations

Particle based cosmic ray detectors are often placed at high altitude locations, because the shower maximum is high in the atmosphere, and radio detectors can also be located on the same sites, so it is important to consider the altitude effect on the radio signal. As we get closer to the shower maximum,
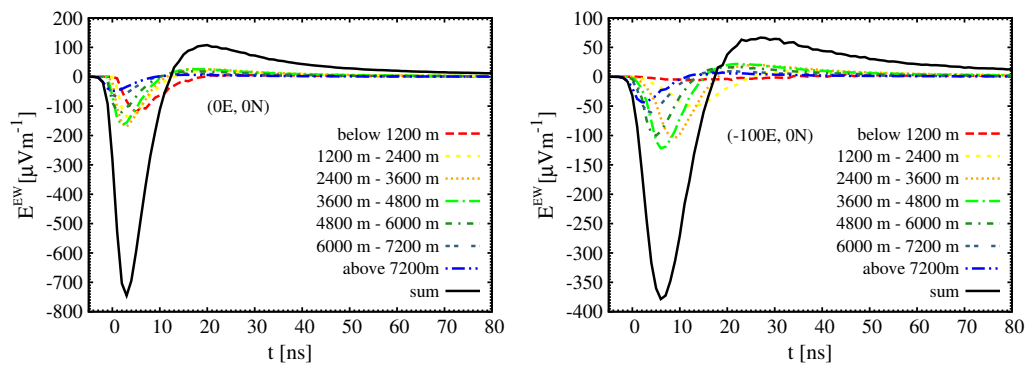
Fig. 6 Contributions from different layers. *Left*: the observation site is at the shower impact center. *Right*: the observation site is 100 m west from it.
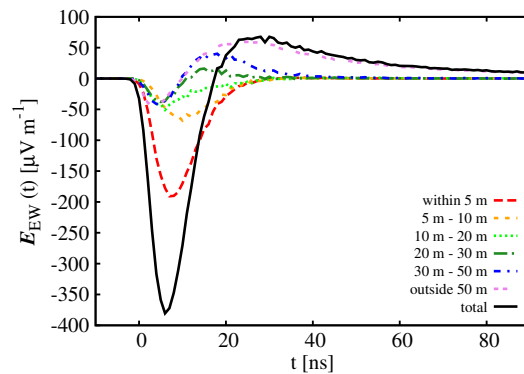
Fig. 7 Contributions at different lateral distances to the shower axis. The intervals are within 5 m, $5 - 10$ m, $10 - 20$ m, $20 - 30$ m, $30 - 50$ m and beyond 50 m.

we may receive stronger emission from this stage. On the other hand, at the higher elevation, the signals from the later stage of the shower are missed.

Figure 8 shows how the peak field strength of the radio pulse varies with elevation of the observation site for a vertical shower at several offset differences from the center on the ground. In all cases, the variation is apparent but not very rapid. In the case of the center of the shower at the ground, the signal strength gradually rises at the beginning and reaches its maximum value at around 4000 m high, where the shower develops to its maximum for a 10^{17} eV cosmic ray. At a still higher altitude, the signal begins to attenuate. In the off center cases, the peak strength drops off with increasing altitude, and for the three off-center distances we computed, the variations have similar dependencies on height. This result shows that if the radio detector array is primarily designed to detect the signal in the area around the center, then there is a little advantage to choosing a site at a high altitude, though it is far less significant than in the case of particle detectors. On the other hand, if the radio array is sensitive enough to detect showers outside the area around the center, then perhaps there is not much advantage to placing the detector at high altitudes.

In Figure 9 we plot the lateral distribution of the radio signal at different elevations for a vertical air shower. There is a slight asymmetry in the lateral distribution along the EW direction about the shower axis, where the signal in the east is stronger. This is caused by the excess of electrons in
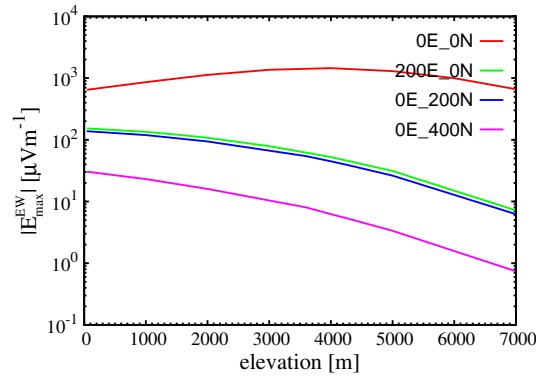
Fig. 8 Elevation dependence of the radio signal. Signals at four locations (center on the ground, 200 m due East of the center, 200 m due North of the center and 400 m due North of the center) are plotted as a function of ground altitude.
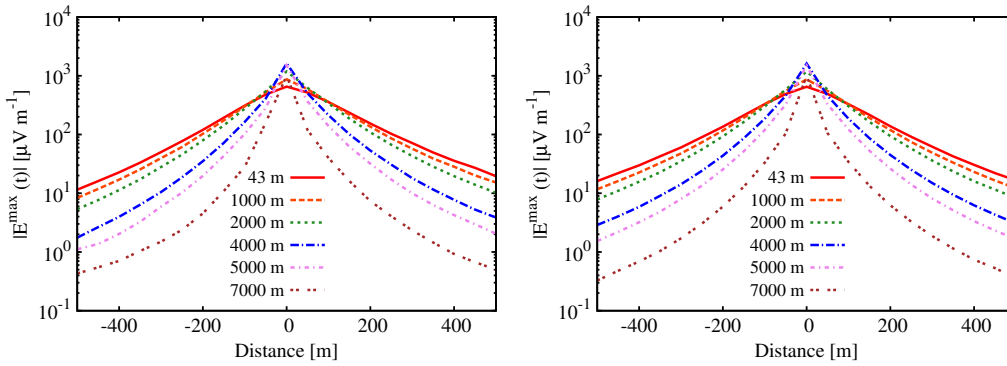
Fig. 9 The peak field strength of the pulse as a function of off-center distance in the EW (*top*) and NS (*bottom*) directions.

the shower, but this does not affect the NS distribution. Close to the shower axis, the peak electric field strength rises with the increase of elevation until about $4000 \, \text{m}$, where the shower reaches the maximum for a 10^{17} eV cosmic ray primary. Away from the shower axis, the strength always decreases with height. The turning point between the *center* and *off-center* is around $50 \, \text{m}$. The radial dependence of the electric field signal is usually parameterized by an exponential function

$$\varepsilon(r) = \varepsilon_{100} \exp(-(r - 100\text{m})/R_0) \,, \tag{22}$$

where ε_{100} is the amplitude at $100 \, \text{m}$ and scale parameter R_0 is usually about 100 to $250 \, \text{m}$, except for some events which have a very large R_0 (Haungs et al. 2009; Apel et al. 2010). We use Equation (22) to fit the lateral distribution in the range $200 - 500 \, \text{m}$ at different elevations, and show the variation of R_0 with height in Figure 10. We can see that R_0 does not change significantly with height.

4.5 Inclined Showers: Dependence on Zenith Angle and Azimuth Angle

So far, we have only considered vertical showers, but inclined showers are of course more common. The inclined showers share some general characteristics with the vertical ones, and now we
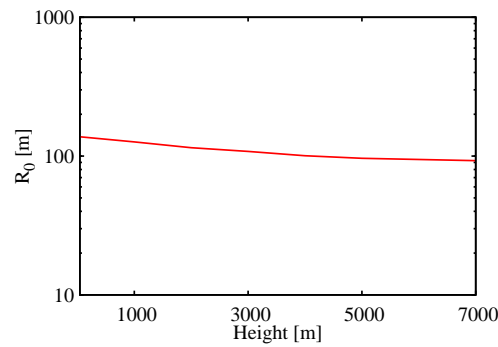
Fig. 10 Elevation dependence of the scale R_0.
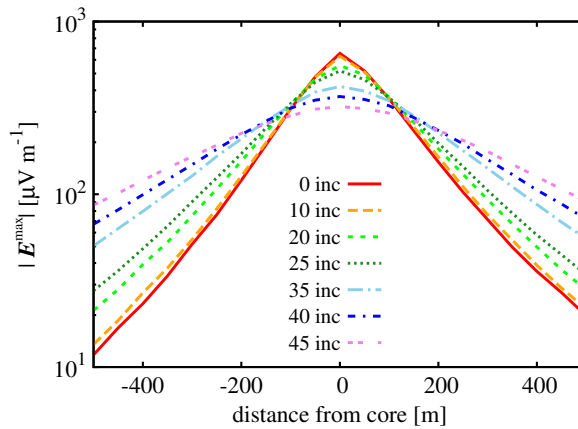
Fig. 11 The radial distribution of the strength of the radio signal under different zenith angles.

will investigate how the behavior of the shower changes as the inclination angle varies. The zenith dependence of the radial distribution is shown in Figure 11. At the shower impact center, the field strength decreases with zenith angle, so the vertical shower has the largest peak strength. However, inclined showers have a broader distribution, so some distance away from the center they may actually have greater field strength.

In Figure 12, we show the contours of the radio emission field strength with different zenith angles, where the shower axis is assumed to be inclined from the direction of east at different angles. Such a spatial distribution could be detected with a phalanx of radio receivers, and we show the distribution for the total strength as well as the polarized electric field along the EW, NS and vertical directions.

For a vertical shower (zenith angle $0°$), the total field strength and the dominant EW polarization components have a distribution that follows concentric ellipses. The NS and vertical polarizations, on the other hand, exhibit asymmetric bimodal structures in this case. This asymmetry is due to the effect of the magnetic field, which breaks the otherwise totally symmetric arrangement in the vertical shower.

With increasing zenith angles, the total field strength and the dominant EW polarization decrease slightly and their elliptical contours become more prolate along the EW direction. The axis of the elliptical contours also becomes longer. At the same time, the bimodal structures in the NS and vertical components change to concentric ellipses and now these components have greater mag-
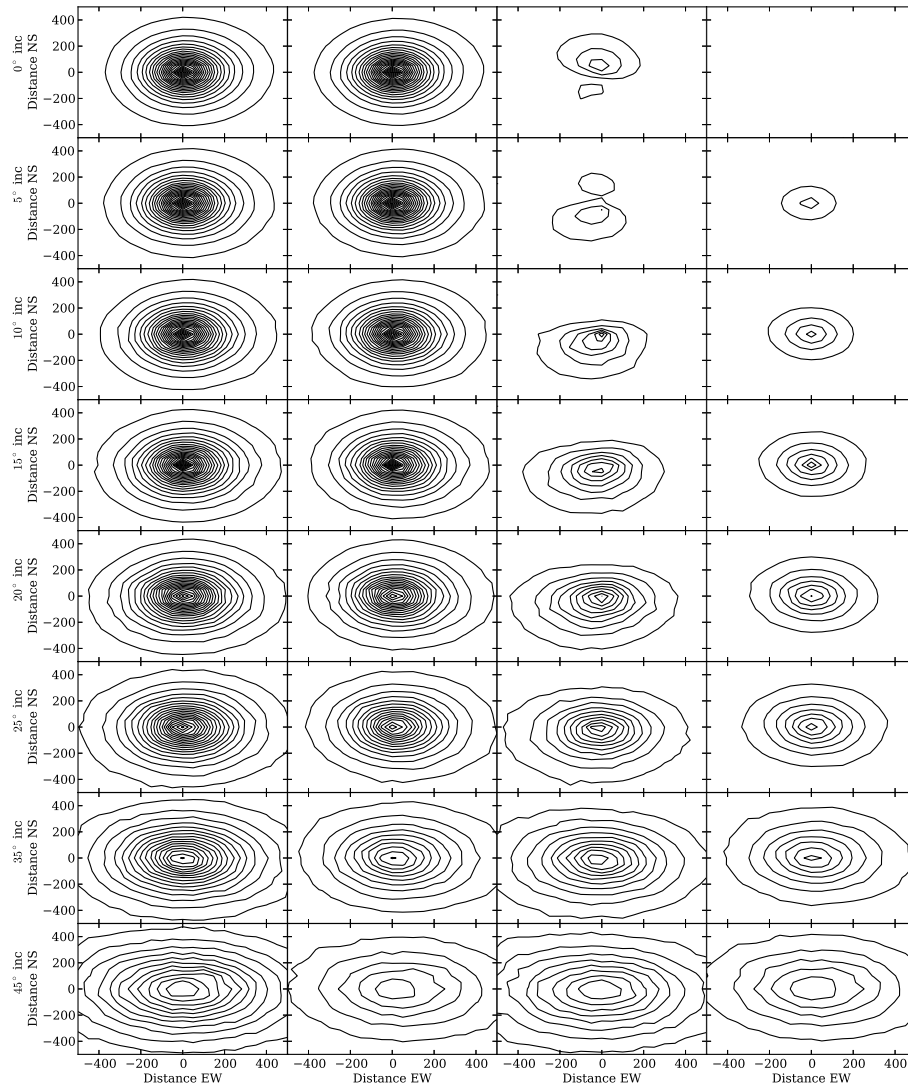
Fig. 12 The contours of unfiltered radio emission under different zenith angles. Columns from left to right: total field strength, the EW polarization, the NS polarization and the vertical polarization. Lines from top to bottom show zenith angles of $0°$, $5°$, $10°$, $15°$, $20°$, $25°$, $35°$ and $45°$ respectively. Contour levels are $25 \ \mu V \ m^{-1}$ apart.

nitudes than the vertical case. Their magnitudes gradually grow. These changes are consistent with our expectation for a cross section oriented at a slant with respect to the shower axis.

The contour maps from different incident azimuth directions in the case of pure geosynchrotron were studied in Huege & Falcke (2005b). Besides elongation of the field strength pattern, they found that the total field strength pattern rotates with the azimuth angle. The measurements of the individual polarization components can be used to directly verify the geosynchrotron origin of the signal in the radio emission.
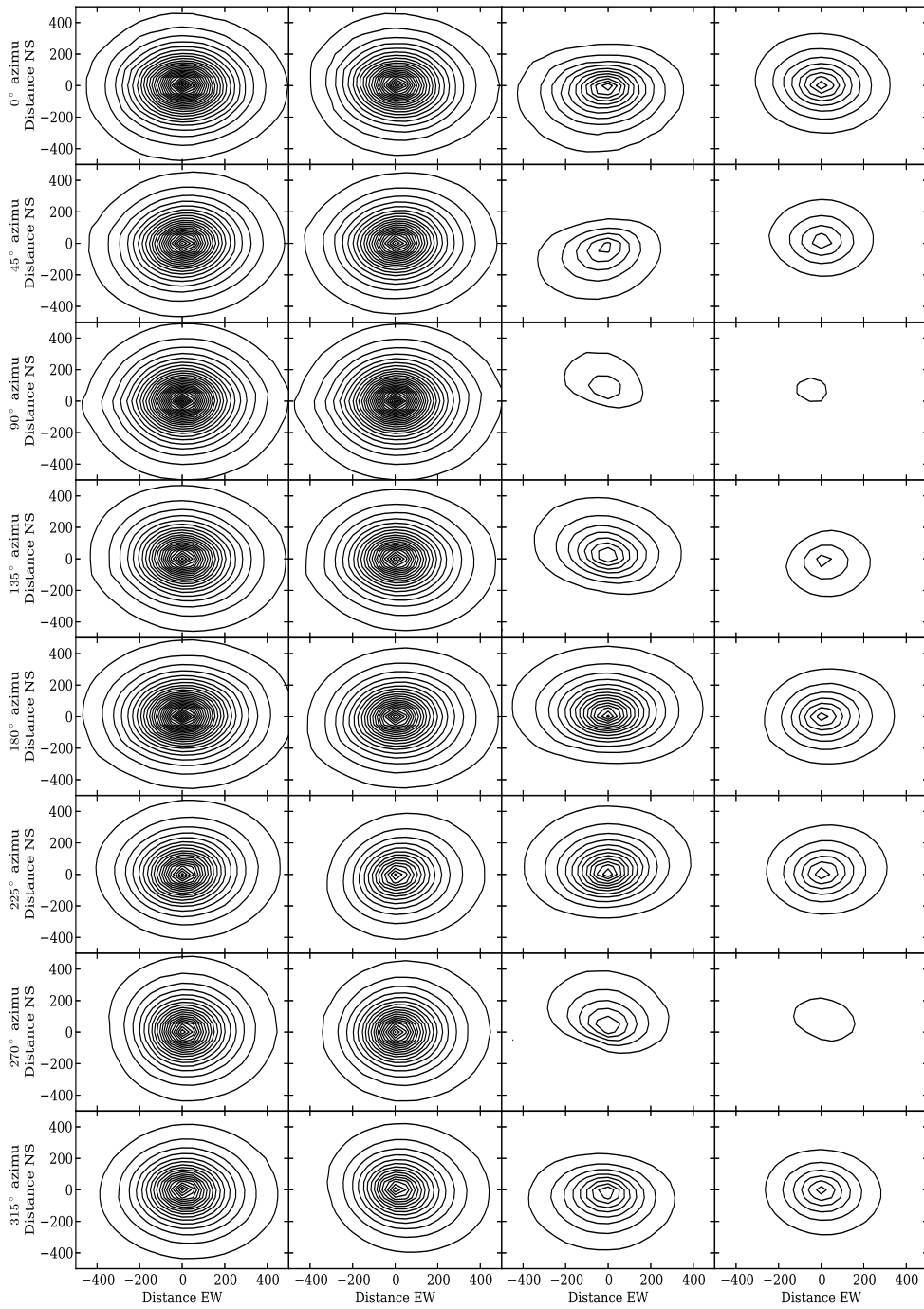
Fig. 13 The contours of unfiltered radio emission for a 20°-inclined shower coming from different incident azimuthal directions. Columns from left to right are respectively the total field strength, the EW polarization, the NS polarization and the vertical polarization. Lines from top to bottom show azimuth angles of 0°, 45°, 90°, 135°, 180°, 225°, 270° and 315° respectively. Contour levels are $25\,\mu\mathrm{V\,m^{-1}}$ apart.

With the inclusion of the charge excess and creation/destruction effects, the situation becomes more complicated. As shown in Figure 13, the contours of the total field strength show concentric ellipses, but there are some slight changes in the orientation of these ellipses which are not very obvious. This is not surprising, because with both the geosynchrotron and creation/destruction emission at work, the geometric relation is more complicated. Again, the NS and vertical polarizations show more irregularity, in some cases with a bimodal pattern.

5 CONCLUSIONS

In this paper, we describe our new Monte Carlo simulation of the radio signal emitted by a cosmic ray extensive air shower. Our basic approach is similar to *REAS2*, using the Monte Carlo method to generate a sample of particles and calculate the field produced by them, but we included the charge excess effects in addition to geosynchrotron radiation. We use step functions in the retarded potentials to represent the creation and destruction of particles. At low frequency, the radiation field can be derived classically. The algorithm of our numerical program is presented which has passed preliminary checks and gives results which are consistent with the ones obtained by others.

We find that when the charge excess effect is included, the radio signal is significantly modified: the magnitude of the signal is substantially reduced, and in the time domain, the pulse EW polarization exhibits a bimodal pattern. This is the most important distinction compared to the previous pure geosynchrotron radiation. The charge excess effect on the frequency spectrum is also considered. The geosynchrotron and charge excess effect, when computed individually, have similar spectra which drop at ~ 100 MHz due to the loss of coherence. At low frequencies, both have a flat spectrum, but when added the two tend to cancel each other and the spectrum also drops at the lower end. These findings are in good agreement with recent results reported in the literature (Huege et al. 2012). We also computed the spectra at different locations. Near the center, the charge excess effect alters the steep spectrum predicted by the pure geosynchrotron mechanism, and the combined spectrum is in agreement with observations. Off the center, the theoretical spectrum is steeper than the observation. This may be due to experimental error or another kind of radiation, such as Čerenkov radiation.

We further apply our program to study the features of the signals. For a vertical shower and near the shower axis, we find that the signal can at any time come from a wide span of different heights, and indeed the layers from different heights could all give sizeable contributions to the total signal, though the shower maximum contributed most. Far off the center, the contribution from the shower maximum dominates, but near the center, layers in the lower altitude could also contribute a large share.

We study the elevation dependence of the signal. At the center of the shower, as the altitude rises, the peak magnitude increases slightly, then drops off if the altitude reaches beyond that of the shower maximum. Off center, it always decreases with increasing altitude. This means that there is a slight advantage to placing the radio array detector at high altitude sites, if the array is designed to detect the radio signal at the center. On the other hand, if the array is sufficiently sensitive to be able to detect the radio emission at a large off-center distance, then there is not much advantage to placing it at high altitudes. Indeed, even in the former case, the advantage is far less obvious than a particle-based detector. We use an exponential function to fit the radial distributions and find R_0 is about 100 m, which is consistent with experimental results.

We then consider inclined showers with different zenith and azimuth angles, and compute the spatial distribution of the signal. We find that the contour lines of signal strength are basically concentric ellipses, but due to the asymmetry of charges, there is an azimuthal asymmetry in the EW polarization even for a vertically-downward air shower. The total field strength and the dominant EW polarization gradually decrease as the zenith angle increases, and the ellipses are elongated. However, the addition of the charge excess effect obscures the signature of the geosynchrotron ef-

fect, so the azimuthal dependence of the total field strength is not apparent. In the NS polarization, the shape is also changed from a unimodal to a bimodal pattern. Our results could act as a useful tool for studying the detection of incoming radio signals.

This paper presents a very basic model of radio emission from a cosmic ray air shower, and some similar results have been obtained previously. Nevertheless, it is useful to verify these results with an independent computation as we did, and to examine how the signal varies with elevation, shower inclination, azimuth angle, etc. Moreover, this is a first step toward an independent, comprehensive numerical study of the problem of air shower radio emission. We are working to improve our model by incorporating more physical effects and implementing more realistic models. We plan to use a shower model generated by a modern Monte Carlo code (e.g. CORSIKA). The effect from the variation of atmospheric refractive index and the corresponding Čerenkov radiation will also be investigated in our subsequent works. We can then investigate showers with different energies and compositions, which will be useful to radio detection experiments.

Appendix A: COORDINATE TRANSFORMATION

In this part, the position and velocity of a charged particle in the reference frame of Earth are related to its relative position in the shower disk. In an incident shower with zenith angle Θ, the center of the disk plane is set to be the origin O' of the (moving) shower coordinates. The X' axis is in the plane of incidence, pointing horizontally outwards, and the Y' axis is in the disk plane and normal to the X' axis on the right hand side. The Z' points upward (see the right panel of Fig. A.1). The relative position of the particle P can be written as

$$\boldsymbol{R}'_r = \begin{cases} r\cos\varphi\cos\Theta \ , \\ r\sin\varphi \ , \\ -r\cos\varphi\sin\Theta \ , \end{cases} \tag{A.1}$$

where r is the distance from the origin O' and φ is the azimuthal angle around the disk plane, which rotates counterclockwisely from the lower part of the shower disk.

The coordinate $\boldsymbol{R}_r$ of P can be transformed from $X'O'Y'$ to the system $XO'Y$,

$$x = x'\cos\Phi - y'\sin\Phi \ , \tag{A.2}$$
$$y = y'\cos\Phi + x'\sin\Phi \ . \tag{A.3}$$

Here in the $XO'Y$ plane, the X and Y axis respectively point to the east and north (see the left figure of Fig. A.1). Φ is the azimuthal angle in the system XOY.

The position of O' in the XYZ system, where the impact center O is set to be the origin, is given by

$$\boldsymbol{R}_{O'} = \boldsymbol{R}_{\mathrm{sf}} \times (R_{\mathrm{sf}} + d)/R_{\mathrm{sf}} \ , \tag{A.4}$$

where $\boldsymbol{R}_{\mathrm{sf}}$ is the position of the center of the shower front in the XYZ system, which is equal to $\boldsymbol{R}'_{\mathrm{sf}} - H\hat{\boldsymbol{e}}_z$, if the impact center is H meters above sea level. Position $\boldsymbol{R}'_{\mathrm{sf}}$ could be evaluated according to the relation between height and atmospheric depth X which is produced by a random
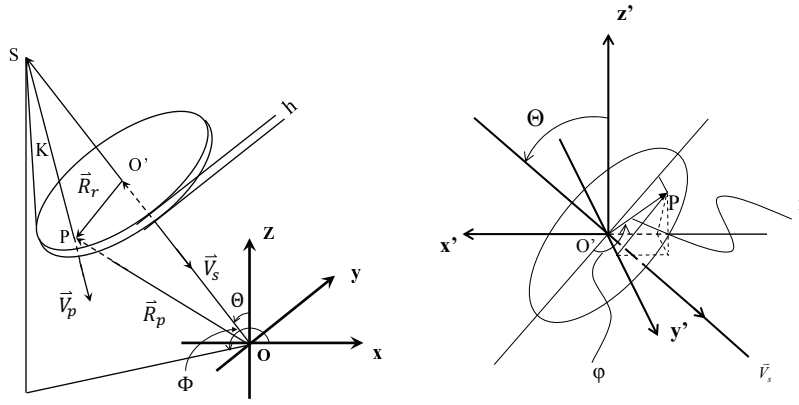
Fig. A.1 *Left*: a sketch of the shower disk in Earth's coordinate system XYZ, with X and Y respectively pointing to the east and north. *Right*: the shower disk in the local system $X'O'Y'$.

number generator in the Monte Carlo code (see Sect. 3.1), and d is the distance from the shower front. The position in system XYZ can be further obtained from the vector relationship

$$\mathbf{R}_{\mathrm{p}} = \mathbf{R}_{O'} + \mathbf{R}_r \ . \tag{A.5}$$

Finally, the absolute position is

$$\mathbf{R}'_{\mathrm{p}} = \mathbf{R}_{\mathrm{p}} + H \, \hat{\mathbf{e}}_z \ . \tag{A.6}$$

Secondary particles are assumed to be distributed within the spherical shell, with radius K equal to 2300 m. Therefore, the direction of their initial velocity is assumed to be radial, i.e.

$$\hat{\mathbf{V}}_{\mathrm{p}} = \frac{\mathbf{R}_{\mathrm{p}} - \mathbf{R}_{\mathrm{s}}}{|\mathbf{R}_{\mathrm{p}} - \mathbf{R}_{\mathrm{s}}|} \ , \tag{A.7}$$

where

$$\mathbf{R}_{\mathrm{s}} = \mathbf{R}_{O'} \times (R_{O'} + K)/R_{O'} \ . \tag{A.8}$$

Appendix B: THE MOTION OF A CHARGED PARTICLE IN A MAGNETIC FIELD

The motion of a single charged particle in a static uniform magnetic field is determined by the Lorentz equation

$$\gamma m \frac{\mathrm{d}\mathbf{V}}{\mathrm{d}t} = -q\mathbf{V} \times \mathbf{B} \ , \tag{B.1}$$

where γ is the Lorentz factor. By applying a cross product with $\mathbf{B}$ on both sides, differentiating it, using Equation (B.1) and the vector identify $\mathbf{B} \times (\mathbf{V} \times \mathbf{B}) = \mathbf{V}B^2 - \mathbf{B}(\mathbf{V} \cdot \mathbf{B})$, we get a second-order differential vector equation

$$\frac{\mathrm{d}^2\mathbf{V}}{\mathrm{d}t^2} + \left(\frac{q\mathbf{B}}{\gamma m}\right)^2 \mathbf{V} - \left(\frac{q}{\gamma m}\right)^2 \mathbf{B}(\mathbf{V} \cdot \mathbf{B}) = 0 \ . \tag{B.2}$$

By applying a dot-product to $\mathbf{B}$ on both sides of the Lorentz equation,

$$\frac{\mathrm{d}(\mathbf{V} \cdot \mathbf{B})}{\mathrm{d}t} = 0 \ , \tag{B.3}$$

i.e. $\mathbf{V} \cdot \mathbf{B} = \text{const}$, so the solution of Equation (B.2) is

$$\mathbf{V}(t) = \mathbf{a}_1 \cos \omega_B t + \mathbf{b}_1 \sin \omega_B t + \frac{\mathbf{B}(\mathbf{V}_0 \cdot \mathbf{B})}{B^2} , \tag{B.4}$$

where $\omega_B^2 = (q\mathbf{B}/\gamma m)^2$ is the gyration frequency of the circular motion and $\mathbf{V}_0$ is the initial velocity. The constants $\mathbf{a}_1$ and $\mathbf{b}_1$ can be determined from the initial conditions,

$$\mathbf{a}_1 = \mathbf{V}_0 - \frac{\mathbf{B}(\mathbf{V}_0 \cdot \mathbf{B})}{B^2} , \qquad \mathbf{b}_1 = \frac{q(\mathbf{a}_1 \times \mathbf{B})}{\gamma m \omega_B} . \tag{B.5}$$

The trajectory of the particle can then be integrated, which is given by

$$\mathbf{X}(t) = \frac{\mathbf{a}_1}{\omega_B} \sin \omega_B t - \frac{\mathbf{b}_1}{\omega_B}(\cos \omega_B t - 1) + \frac{\mathbf{B}(\mathbf{V}_0 \cdot \mathbf{B})}{B^2} t + \mathbf{X}_0 , \tag{B.6}$$

where $\mathbf{X}_0$ is the initial position.

References

Agnetta, G., Ambrosio, M., Aramo, C., et al. 1997, Astroparticle Physics, 6, 301

Allan, H. R. 1971, Prog. in Element. Part. and Cos. Ray Phys., 10, 171

Alvarez-Muñiz, J., Carvalho, W. R., & Zas, E. 2012, Astroparticle Physics, 35, 325

Apel, W. D., Arteaga, J. C., Asch, T., et al. 2010, Astroparticle Physics, 32, 294

Apel, W. D., Arteaga, J. C., Bähren, L., et al. 2013, arXiv:1303.7080

Ardouin, D., Belletoile, A., Berat, C., et al. 2009, Astroparticle Physics, 31, 192

Ardouin, D., Bellétoile, A., Charrier, D., et al. 2006, Astroparticle Physics, 26, 341

Ardouin, D., Cârloganu, C., Charrier, D., et al. 2011, Astroparticle Physics, 34, 717

Askaryan, G. A. 1962, Journal of the Physical Society of Japan Supplement, 17, C257

Askar'yan, G. A. 1965, Soviet Journal of Experimental and Theoretical Physics, 21, 658

de Vries, K. D., Scholten, O., & Werner, K. 2012, Nuclear Instruments and Methods in Physics Research A, 662, 175

de Vries, K. D., van den Berg, A. M., Scholten, O., & Werner, K. 2010, Astroparticle Physics, 34, 267

Dova, M. T., Epele, L. N., & Mariazzi, A. G. 2003, Astroparticle Physics, 18, 351

Falcke, H., Apel, W. D., Badea, A. F., et al. 2005, Nature, 435, 313

Greiner, W. 1998, Classical Electrodynamics, Classical Theoretical Physics Series (Springer Verlag)

Greisen, K. 1960, Annual Review of Nuclear and Particle Science, 10, 63

Griffiths, D. J., & College, R. 1999, Introduction to Electrodynamics (3rdn., Benjamin Cummings, Prentice Hall Upper Saddle River, NJ)

Haungs, A., Apel, W. D., Arteaga, J. C., et al. 2009, Nuclear Physics B Proceedings Supplements, 196, 297

Heck, D., Knapp, J., Capdevielle, J. N., Schatz, G., & Thouw, T. 1998, CORSIKA: a Monte Carlo Code to Simulate Extensive Air Showers., eds. Heck, D., Knapp, J., Capdevielle, J. N., Schatz, G., & Thouw, T. Forschungszentrum Karlsruhe GmbH, Karlsruhe (Germany)

Huege, T., & Falcke, H. 2003, A&A, 412, 19

Huege, T., & Falcke, H. 2005a, A&A, 430, 779

Huege, T., & Falcke, H. 2005b, Astroparticle Physics, 24, 116

Huege, T., Ludwig, M., Scholten, O., & de Vries, K. D. 2012, Nuclear Instruments and Methods in Physics Research A, 662, 179

Huege, T., & Pierre Auger Collaboration 2010, Nuclear Instruments and Methods in Physics Research A, 617, 484

Huege, T., Ulrich, R., & Engel, R. 2007, Astroparticle Physics, 27, 392

Jackson, J. D. 1998, Classical Electrodynamics (3rd edn; Wiley VCH)

James, C. W., Falcke, H., Huege, T., & Ludwig, M. 2011, Phys. Rev. E, 84, 056602

Jelley, J. V., Fruin, J. H., Porter, N. A., et al. 1965, Nature, 205, 327

Kahn, F. D., & Lerche, I. 1966, Royal Society of London Proceedings Series A, 289, 206

Kamata, K., & Nishimura, J. 1958, Progress of Theoretical Physics Supplement, 6, 93

Knurenko, S. P., Kozlov, V. I., Petrov, Z. E., & Pravdin, M. I. 2013, Journal of Physics Conference Series, 409, 012070

Ludwig, M., & Huege, T. 2011, Astroparticle Physics, 34, 438

Marin, V. 2013, in American Institute of Physics Conference Series, 1535, eds. R. Lahmann, T. Eberl, K. Graf, et al., 148 (arXiv:1212.1348)

Marin, V., & Revenu, B. 2012, Astroparticle Physics, 35, 733

Martineau-Huynh, O., Ardouin, D., Cârloganu, C., et al. 2012, Nuclear Instruments and Methods in Physics Research A, 662, 29

Melrose, D. B., & McPhedran, R. C. 2005, Electromagnetic Processes in Dispersive Media (Cambridge: Cambridge Univ. Press)

Nigl, A., Apel, W. D., Arteaga, J. C., et al. 2008, A&A, 488, 807

Roh, S., Kim, J., Ryu, D., et al. 2013, Astroparticle Physics, 44, 1 (arXiv:1301.5060)

Scholten, O., Werner, K., & Rusydi, F. 2008, Astroparticle Physics, 29, 94

Schoorlemmer, H., & Pierre Auger Collaboration 2012, Nuclear Instruments and Methods in Physics Research A, 662, 134

Schröder, F. G., Apel, W. D., Arteaga-Velázquez, J. C., et al. 2013, in American Institute of Physics Conference Series, 1535, eds. R. Lahmann, T. Eberl, K. Graf, et al., 78

Sciutto, S. J. 1999, arXiv:astro-ph/9911331

Werner, K., de Vries, K. D., & Scholten, O. 2012, Astroparticle Physics, 37, 5

Werner, K., & Scholten, O. 2008, Astroparticle Physics, 29, 393